Atmos. Meas. Tech. Discuss., 8, 4325–4345, 2015
www.atmos-meas-tech-discuss.net/8/4325/2015/
doi:10.5194/amtd-8-4325-2015

Atmospheric Measurement Techniques Discussions
Open Access

Intercomparing CO_2 amounts from dispersion modeling, 1.6 µm differential absorption lidar and open path FTIR at a natural CO_2 release at Caldara di Manziana, Italy

M. Queißer[1], D. Granieri[1], M. Burton[1,*], A. La Spina[2], G. Salerno[2], R. Avino[3], and L. Fiorani[4]

[1]Istituto Nazionale di Geofisica e Vulcanologia (INGV), Sezione di Pisa, Pisa, Italy
[2]Istituto Nazionale di Geofisica e Vulcanologia (INGV), Sezione di Catania, Catania, Italy
[3]Istituto Nazionale di Geofisica e Vulcanologia (INGV), Sezione di Napoli, Napoli, Italy
[4]Diagnostics and Metrology Laboratory, Italian National Agency for New Technologies, Energy and Sustainable Economic Development (ENEA), Frascati, Italy
[*]now at: School of Earth, Atmospheric and Environmental Sciences, University of Manchester, Manchester, UK

Received: 18 March 2015 – Accepted: 12 April 2015 – Published: 29 April 2015

Correspondence to: M. Queißer (manuelqueisser@web.de)

Published by Copernicus Publications on behalf of the European Geosciences Union.

Abstract

We intercompare results of three independent approaches to quantify a vented CO_2 release at a strongly non-uniform CO_2 Earth degassing at Caldara di Manziana, central Italy. An integrated path differential absorption lidar prototype and a commercial open path FTIR system were measuring column averaged CO_2 concentrations in parallel at two different paths. An Eulerian gas dispersion model simulated 3-D CO_2 concentration maps in the same area, using in situ CO_2 flux input data acquired at 152 different points. Local processes the model does not account for, such as small-scale and short-lived wind eddies, govern CO_2 concentrations in the instrument measurement paths. The model, on the other hand, also considers atmospheric effects that are out of the field of view of the instruments. Despite this we find satisfactory agreement between modeled and measured CO_2 concentrations under certain meteorological conditions. Under these conditions the results suggest that an Eulerian dispersion model and optical remote sensing can be used as an integrated, complementary monitoring approach for CO_2 hazard or leakage assessment. Furthermore, the modeling may assist in evaluating CO_2 sensing surveys in the future. CO_2 column amounts from differential absorption lidar are in line with those from FTIR for both paths with a mean residual of the time series of 44 and 34 ppm, respectively. This experiment is a fundamental step forward in the deployment of the differential absorption lidar prototype as a highly portable active remote sensing instrument probing vented CO_2 emissions, including volcanoes.

1 Introduction

Not only does subaerial CO_2 Earth degassing affect the global geochemical carbon cycle (Burton et al., 2013), but it may also pose a threat to human health in its vicinity, e.g., near volcanoes (Farrar et al., 1995; Hansell and Oppenheimer, 2004).

Central and southern Italy in particular is characterized by strong natural CO_2 degassing that accounts for 10 % of the global CO_2 released by subaerial volcanoes

AMTD
8, 4325–4345, 2015

(Chiodini et al., 2004). Caldara di Manziana (CdM, Fig. 1a) represents one of the strongest of those degassing sites. CdM was probably formed by a hydrothermal explosion (Rogie et al., 2000) and still preserves the shape of an ancient explosion crater with an almost flat bottom and rims elevated a few tens of meters.

A means to assess the gas hazard in such areas is the quantification of the CO_2 release and the investigation of the CO_2 dispersion into the atmosphere through numerical modeling (Costa et al., 2008; Chiodini et al., 2010). Here we intercompare modeled and measured CO_2 amounts from open path FTIR spectrometry (OP-FTIR) and 1.6 µm differential absorption lidar (DIAL) at CdM for the following two reasons.

Firstly, the DIAL is a prototype that currently undergoes first validation surveys. In this context, the well-established OP-FTIR served as a reference instrument for the DIAL. The second motivation is to explore whether for the given situation an Eulerian dispersion model is able to simulate CO_2 amounts that compare to measured CO_2 concentrations. So far we know of only little and limited work on directly comparing modeled and measured volcanic CO_2 amounts (e.g., Granieri et al., 2013, 2014). While both the instruments measure column averaged CO_2 concentrations the model uses input data from point measurements. For the background atmosphere agreement between point and path averaged CO_2 amounts is expected (e.g., Gibert et al., 2008). In this case, using input data from point measurements to simulate column averaged CO_2 amounts that are in line with measured CO_2 column amounts can assumed to be straightforward. At CdM, however, we are sensing a highly non-uniform, non-steady CO_2 concentration, comprising of both diffuse and vented CO_2 degassing, which is challenging this kind of comparison and thus makes it particularly interesting.

2 Instruments and methods

OP-FTIR is an established remote sensing technique to measure CO_2 path amounts, including volcanic CO_2 (Naughton et al., 1969; Burton et al., 2000). The OP-FTIR used is a MIDAC M4406-S (MIDAC Corporation, Irvine, USA) with a ~ 20 mrad field of view

AMTD
8, 4325–4345, 2015

(FOV). Other main components are the Stirling-cooled MCT detector, which is sensitive between 600 and 5000 cm^{-1} and allows operation without liquid nitrogen cooling (e.g., La Spina et al., 2010), a 0.5 cm^{-1} resolution mid-infrared interferometer, the signal-processing electronics and an infrared (IR) light source.

The IR source is located at the other end of the open measurement path and can be either natural, e.g., volcanic magma, or artificial. The measurements at CdM were performed in bistatic active mode using a high emissivity, 24 W SiC element operating at a temperature of ∼ 1200 K placed at the focus of a parabolic reflector with 120 mm diameter. Light from the source traverses the measurement column and enters the interferometer. As one of the interferometer mirrors is translated an interferogram is being produced, which is Fourier transformed to yield an absorption spectrum. Through fitting the latter with a forward modeled spectrum the path averaged CO_2 concentration can be inverted for (Burton et al., 1998). The OP-FTIR provides corresponding CO_2 concentrations on average every 22 s. The necessity of aligning the instrument with a light source at the end of the path limits the flexibility of the approach, for instance, when employed at a volcanic site. Many volcanoes are quiescent and thus offer no magma as light source and may otherwise pose a challenging environment to align the OP-FTIR with an artificial IR source, e.g., due to opaque or toxic volcanic gases. Even at good visibility alignment becomes impractical at ranges beyond 200 m.

To have an instrument deployable at volcanoes that overcomes these drawbacks we are developing a DIAL in the framework of the European Research Council funded project CO_2Volc, which as an active remote sensing technique carries its own light source. The prototype is based on integrated path differential absorption (IPDA, Amediek et al., 2008; Kameyama et al., 2009; Dobler et al., 2013). As a dedicated volcanology tool the instrument is geared towards maximum compactness and transportability in the field. The compact DIAL prototype is described in detail in Queißer et al. (2015). Table 1 summarizes its key parameters. The instrument uses two narrow line width fiber lasers (NKT Photonics, Birkerød, Denmark) operating at two corresponding wavelengths followed by a fiber amplifier stage. The wavelength pair was chosen following

AMTD
8, 4325–4345, 2015

Amediek et al. (2008). The ON wavelength (1572.992 nm) corresponds to a rotational line of the vibrational transition $00^0 0 \rightarrow 22^0 1$ and hence to a local CO_2 absorption maximum of CO_2, while for the OFF wavelength (1573.160 nm) there is negligible CO_2 absorption (Rothman et al., 2012). Photons of one wavelength at a time are alternatingly emitted at a 1 kHz switching rate. The laser light transverses the measurement column, is backscattered by a hard target, such as the ground, traverses the path again and is received by a commercial Schmidt–Cassegrain telescope with 200 mm diameter. A detection unit comprising of a PIN photodiode and a high gain transimpedance amplifier converts the photon flux to a voltage that is being digitized at 50 kSamples s^{-1} with high resolution (24-bit). By computing the ratio of the received light intensities associated with the ON and the OFF wavelengths we obtain the differential optical depth. The latter along with knowledge of the CO_2 absorption cross-section, moist air number density and the path length permits to directly retrieve the path averaged CO_2 concentration. The CO_2 absorption cross-section is calculated using spectroscopic data from the HITRAN 2012 database as well as air temperature and pressure data. Temperature, pressure and relative humidity needed for the air number density are taken from a meteorological station mounted at the edge of CdM (Fig. 1a).

The integration time of the DIAL per measured CO_2 concentrations value is 1 s per wavelength, so 2 s in total, corresponding to 50 000 acquired samples for the ON and 50 000 samples for the OFF wavelength. In the post processing the data are normalized by the transmitted signal strength to correct for laser power fluctuations and averaged to arrive at a mean intensity ratio, yielding a CO_2 concentration value each ~ 3 s. Depending on the atmospheric state, we find the serial wavelength emission scheme to be quite susceptible to atmospheric turbulences (Queißer et al., 2015). Consequently, to mitigate the associated scintillation noise statistical dependence of subsequent data is reduced by using only a fraction of the data and skipping adjacent data following Grant et al. (1988). We use data chunks of up to 10 ms s^{-1}, leaving 99 ms in between the chunks.

AMTD
8, 4325–4345, 2015

The distance between the OP-FTIR and the IR source was 49 m and defined the length of the measurement column (path #1, Fig. 1a). Figure 1a also shows a second path of 126 m length (path #2) we will refer to further below. Path #1 included the water pool (CO_2 vent) at its end, which represents the target CO_2 concentration probed and also the strongest vented CO_2 emission for both paths. While the OP-FTIR line of sight ran 0.5 m above ground, the DIAL stood 1 m above ground aiming at the floor just behind the IR source, hence its optical axis crossed the OP-FTIR axis half way (Fig. 1b). As the instruments were placed side by side, the lines of sights enclosed an angle of the order of 10 mrad, crossing each other at the IR source.

The CO_2 concentrations at CdM strongly depend on how the CO_2 disperses. We performed numerical simulations of CO_2 dispersion using the Eulerian DISGAS code (DISpersion of GAS, Costa et al., 2005; Granieri et al., 2014). DISGAS is coupled with the mass-consistent diagnostic wind model (DWM, Douglas and Kessler, 1990), which can describe wind fields over complex topography. The model is able to reproduce atmospheric dispersion of a dense gas cloud released by point sources or diffuse sources, accounting for topographic effects, soil-cover types, variations of atmospheric conditions and wind direction. The spatial distribution of the CO_2 sources is a very significant modeling input. To obtain it we acquired in situ CO_2 fluxes at 152 points throughout CdM (Fig. 1a) using the accumulation chamber technique (Chiodini et al., 1996; Carapezza and Granieri, 2004). From these measurements we derive the total flux as well as a soil CO_2 flux map using the sequential Gaussian simulation procedure (sGs, Deutsch and Journel, 1998), following the approach by Cardellini et al. (2003). Further input data are the topography, terrain roughness as well as meteorological data, such as wind speed, wind direction, air pressure and temperature taken from the meteorological station. DISGAS outputs air CO_2 concentrations at horizontal x, y points and at heights selected by the user, i.e., it produces a 3-D map. The computational domain is 1.0 km × 1.0 km with an x and y grid spacing of 10 m. Each CO_2 concentration is expressed as a value in excess above the local background CO_2 concentration of 370 ppm, as measured during the fieldwork far from the main degassing

AMTD
8, 4325–4345, 2015

area. Time-lapse concentration 3-D maps are computed for every 2 min, constrained by the maximum acquisition rate of the meteorological station.

From the 3-D concentration maps for each time step we derive spatial mean CO_2 concentrations by averaging values along the grid coordinates that are associated with the line of sight of the instruments and at a fixed height of 0.5 m above ground. The resulting mean CO_2 concentrations are directly compared with the path averaged CO_2 concentrations measured by DIAL and OP-FTIR.

3 Results and discussion

3.1 Modeling results

We find a large spatial variability of soil CO_2 flux, between 4 to 27 500 $g\,m^{-2}\,d^{-1}$, with an average of 890 $g\,m^{-2}\,d^{-1}$. The average total CO_2 output from 100 sGs simulations is $222 \pm 40\,t\,d^{-1}$, with the strongest emissive areas located in the central and northern portion of the CdM crater floor (Fig. 2). Highest values were measured in the vicinity of the water pool (CO_2 vent, Fig. 2) where we estimated an emission of 6.3 $t\,d^{-1}$ of CO_2 through measurement of the air CO_2 concentration gradient above the pool.

Figure 3a shows one of the simulated time-lapse air CO_2 concentrations maps for 15 October 2014, 16:00 CET, at 0.5 m height above ground. The wind was blowing from 235° N, which corresponds quasi to the mean direction until 16:00 CET. The model suggests higher CO_2 concentrations in the northern sector of CdM. The NE inner wall of the crater likely obstructs the dispersion of the plume. Figure 3b shows a map for 30 min after, when the mean wind direction veered to E (~ 90° N) and remained constant until the end of the recording. The CO_2 plume is stretched towards the open western side of the caldera. Consequently, the CO_2 concentration lowers inside the crater.

In contrast to this steady wind scenario, Fig. 3c shows a snapshot of the CO_2 concentrations during the morning of the following day, on 16 October, when the wind direction was fluctuant between 120 to 290° N, with a dominant direction of ca. 203° N.

AMTD
8, 4325–4345, 2015

3.2 Comparing measured CO_2 concentrations with each other

Figure 4a presents the measurement results between 15:50 and 17:00 (CET), 15 October 2014 along with the simulated CO_2 concentrations that are associated with the model scenario Fig. 3a and b are referring to. The DIAL started recording when the wind direction was already changing (around 16:00 CET). After 16 min it was paused to increase the integration time from 2 to 4 s, thus the gap in the time series.

The CO_2 concentrations from OP-FTIR are on average 430 ppm above the local background value and in line with those from the DIAL. Since the temporal resolution of the DIAL is on average 7 times higher than the FTIR sample spacing the FTIR series is smoother. Nonetheless, the DIAL series trend follows the OP-FTIR trend, that is, it slightly decreases, with a mean concentration 30 ppm higher during the first 10 min of DIAL recording than during the following 10 min. To obtain a measure for the match between OP-FTIR and DIAL result we compute the residuals of the OP-FTIR series relative to the DIAL series. Taking the mean of the residuals yields 44 ppm.

The FOV of the DIAL is $\sim 1/20$ of the FTIR FOV, sensing a much smaller slice of the CO_2 vent. Consequently, a number of short lived CO_2 dispersion effects and heterogeneities of the degassing that contributed to the FTIR signal have not been sensed by the DIAL. This explains why at places large amplitude, small time-scale fluctuations are not coinciding. Disagreement of this sort may furthermore be due to the different angles under which both instruments were probing the gas plume.

Due to a malfunctioning of the DIAL reference detecting unit that occurred in the field we did not normalize the transmitted signal for power fluctuations, which increases the uncertainty of the resulting CO_2 concentrations. Therefore, the SD in Fig. 4b also includes fluctuations of the laser power. The latter may fluctuate by up to 1 % of its mean corresponding to an uncertainty of up to 255 ppm in excess of the background concentration, which would make laser power fluctuations by far the highest source of uncertainty. However, the match with the FTIR data indicates that fluctuations of this magnitude were absent during the measurement.

AMTD
8, 4325–4345, 2015

The serial wavelength switching scheme of the DIAL may lead to higher data variability at the presence of atmospheric dynamics, such as turbulences or lifted water droplets from the CO_2 vent. As a consequence, the latter may cause spike-like errors, such as near 16:09 CET (Fig. 4a and b). In this regard, the experiment was important for the further development of the DIAL as it showed evidence that at the current serial wavelength switching scheme atmospheric effects such as these may strongly affect its performance. Owing to the flat terrain, noise due to atmospheric turbulence was significantly lower than at a previous test with the same prototype (Queißer et al., 2015), but in general still contributed to the uncertainty of the CO_2 amount (Fiorani and Durieux, 2001). To minimize common mode noise caused by atmospheric variability the DIAL is currently modified to allow for simultaneous sensing of ON and OFF related signal.

3.3 Comparing measured with simulated CO_2 concentrations

For the beginning of the comparison, both the CO_2 concentrations from OP-FTIR and from DIAL agree well with those predicted by DISGAS (Model, Fig. 4a). In particular, the simulated CO_2 concentrations decrease during the first ~ 20 min coinciding with the major change in wind direction. Remarkably, the CO_2 concentrations from OP-FTIR and DIAL do so as well. However, after 16:10 CET their mean remains quasi constant and roughly 150 ppm above the modeled values. Given the model grid spacing of 10 m and since the simulated CO_2 concentration was very non-uniform after the wind direction had changed (Fig. 3b), even a small mismatch between instrumental FOV and the model spatial domain may have led to the systematic discrepancy we see after 16:10 CET in Fig. 4a. Under this conditions spatial mismatch coming from the GPS coordinates of the instruments, which is of the order of 3 m, becomes relevant too.

For the higher time series frequencies, a great deal of the disagreement can be attributed to the different domains of the approaches, in particular differences in temporal and spatial resolution between numerical model and instruments. Vented emissions possess dynamics that are challenging to model. Rather than being in a constant flow the main CO_2 vent is characterized by pulsed degassing, which undoubtedly con-

AMTD
8, 4325–4345, 2015

tributed to the CO_2 concentration measured by the instruments and partly explains peaks and troughs in the time series.

The difference in tempo-spatial resolution is furthermore associated with a different sensitivity of the model with respect to the instruments to relatively rapid and small-scale changes in atmospheric conditions. The model assumes a simultaneous effect of 152 emissive points spread over CdM, including the strong contribution of the CO_2 vent. These points are roughly 50 m apart and only a couple of them are located close to the instrument measurement paths. Furthermore, the model has a spatial resolution of 10 m horizontally and 0.5 m vertically. The instruments, on the other hand, are designed to sense CO_2 concentrations within a small solid angle corresponding to tens of cm at the end of their path, thus sensing a rather narrow cone, which is slicing the target CO_2 vent. Clearly, they are expected to be sensitive to small-scale fluctuations of CO_2 concentration the model does not account for. For instance, while the CO_2 vent is associated with one grid point only, in the area above the vent CO_2 concentrations are governed by a number of short-lived processes, such as lateral eddies pushing up air.

Furthermore, the model has a temporal resolution of 2 min, i.e., the acquisition rate of the meteorological station. In contrast, the acquisition times of the DIAL and the OP-FTIR are of the order of seconds. DISGAS is geared towards resolving variations in CO_2 concentration linked to atmospheric pressure and temperature over hourly or diurnal time scales. It performs worse at capturing sudden CO_2 fluctuations over relatively short time scales of seconds to minutes associated with changes in wind speed and wind direction. The instruments do this very well.

Despite the limitations of the Eulerian DISGAS code to reproduce dispersion in the proximity of the gas source, the numerical simulations provide a satisfactory agreement with the measurements along path #1. Note that apart from the change in wind direction the wind field for path #1 was quite steady and thus the atmosphere rather stable.

Figure 4a also shows the result of the second comparison associated with the morning after where the atmospheric situation was quite different (Fig. 3c). The path was 126 m long (path #2, Fig. 1a) and included the main CO_2 vent as well. The OP-FTIR

AMTD
8, 4325–4345, 2015

and the DIAL time series agree reasonably well, with a mean residual of the OP-FTIR series relative to the DIAL series of 34 ppm. As for path #1, the maximum simulated CO_2 concentrations reach 800 ppm. However, while the latter have a mean of 480 ppm, the instrumental CO_2 concentrations are around 200 ppm only and so the match between instrumental and model result is poor.

To analyze this we consider the result of a second simulation, which accounts for the flux around the CO_2 vent only, therefore representing the lower limit of modeled CO_2 concentration (Model CO_2 vent, Fig. 4a). For path #1 this result is on average closer to the default modeling scenario than for path #2, suggesting that the path #1 modeling result is dominated more by the CO_2 vent than the path #2 modeling result. An explanation can be found by confronting the path lengths and the atmospheric stability. Unlike for path #1 no major change in wind direction occurred during the acquisition. However, as mentioned above, the wind direction was swiftly fluctuating around its mean suggesting a less stable atmosphere during the path #2 acquisition. This is consistent with the fact that the recording took place in the morning. In the morning, the near-surface layer of the atmosphere is characterized by positive buoyancy due to the soil heating as opposed to the later afternoon when air is negatively buoyant and turbulences are reduced. This suggests that effects contributing to the instruments responses are associated with tempo-spatial scales below the model resolution. For instance, sampling the wind every 2 min was likely missing important changes in the wind direction that, however, governed the CO_2 distribution sensed by the instruments.

In addition, unlike for the shorter path #1, the target CO_2 vent less dominates the CO_2 concentration. So under the given turbulent atmospheric conditions the measured CO_2 concentrations were strongly governed by small-scale dispersion processes and the vent concentration was being perturbed more by diffuse CO_2 than at path #1. These conditions are harder to account for by DISGAS than those for path #1 and so the agreement between measurements and model is worse than for path #1.

In sum, the outcome of the comparison suggests that the match between modeled result and instrumental result is better for stable atmospheric conditions and when

AMTD
8, 4325–4345, 2015

the target vent probed by the instruments dominates the CO_2 concentration within the measurement volume. The result for path #2 illustrates the limits of DISGAS for this application.

4 Conclusions

We have retrieved and intercompared column averaged CO_2 concentrations at a vented CO_2 release at Caldara di Manziana from three approaches, that is, by

1. direct measurement with DIAL,
2. inversion of absorption spectra from OP-FTIR and
3. computing spatial means of CO_2 concentrations from gas dispersion modeling that used in situ input flux data from point measurements.

The DIAL and the OP-FTIR results are in reasonable agreement with each other. This experiment was an important validation step for the DIAL prototype as it gave valuable input for its further development. In particular, a simultaneous wavelength emission scheme is currently implemented to minimize common mode noise related to atmospheric dynamics.

The low frequency trend of the measured CO_2 concentration time series is in line with CO_2 concentrations from a gas dispersion model under certain conditions. The tempo-spatial resolution of the model must be able to account for significant changes in the wind field at the measurement path of the instruments. For stable atmospheric conditions and if the CO_2 amounts in the probed path are dominated by the target CO_2 concentration an Eulerian dispersion model such as DISGAS is able to produce path averaged CO_2 concentrations compatible to those measured. In this case an Eulerian dispersion model and optical remote sensing represent complementary techniques for monitoring non-uniform CO_2 degassing. Furthermore, we deem this combination to be

AMTD
8, 4325–4345, 2015

useful for interpretation and analysis of data acquired with the DIAL in CO_2 sensing surveys at volcanoes planned in the future.

Acknowledgements. This work is part of the CO_2Volc project financed by the European Research Council Grant 279802. More information can be found under http://CO2volc.pi.ingv.it.

References

Amediek, A., Fix, A., Wirth, M., and Ehret, G.: Development of an OPO system at 1.57 µm for integrated path DIAL measurement of atmospheric carbon dioxide, Appl. Phys. B, 92, 295–302, 2008.

Burton, M.: Remote Sensing of the Atmosphere Using Fourier Transform Spectroscopy, Ph. D. thesis, University of Cambridge, Cambridge, UK, 1998.

Burton, M. R., Oppenheimer, C., Horrocks, L. A., and Francis, P. W.: Remote sensing of CO_2 and H_2O emission rates from Masaya volcano, Nicaragua, Geology, 28, 915–918, 2000.

Burton, M. R., Sawyer, G. M., and Granieri, D.: Deep carbon emissions from Volcanoes, Rev. Mineral. Geochem., 75, 323–354, 2013.

Carapezza, M. L. and Granieri, D.: CO_2 soil flux at Vulcano (Italy): comparison of active and passive methods, Appl. Geochem., 19, 73–88, 2004.

Cardellini, C., Chiodini, G., and Frondini, F.: Application of stochastic simulation to CO_2 flux from soil: mapping and quantification of gas release, J. Geophys. Res., 108, 2425, doi:10.1029/2002JB002165, 2003.

Chiodini, G., Frondini, F., and Raco, B.: Diffuse emission of CO_2 from the Fossa crater, Vulcano Island (Italy), B. Volcanol., 58, 41–50, 1996.

Chiodini, G., Cardellini, C., Amato, A., Boschi, E., Caliro, S., Frondini, F., and Ventura, G.: Carbon dioxide Earth degassing and seismogenesis in central and southern Italy, Geophys. Res. Lett., 31, L07615, doi:10.1029/2004GL019480, 2004.

Chiodini, G., Granieri, D., Avino, R., Caliro, S., Costa, A., Minopoli, C., and Vilardo, G.: Non-volcanic CO_2 Earth degassing: case of Mefite d'Ansanto (southern Apennines), Italy, Geophys. Res. Lett., 37, L11303, doi:10.1029/2010GL042858, 2010.

Costa, A., Macedonio, G., and Chiodini, G.: Numerical model of gas dispersion emitted from volcanic sources, Ann. Geophys., 48, 805–815, 2005, http://www.ann-geophys.net/48/805/2005/.

AMTD
8, 4325–4345, 2015

Costa, A., Chiodini, G., Granieri, D., Folch, A., Hankin, R. K. S., Caliro, S., Avino, R., and Cardellini, C.: A shallow-layer model for heavy gas dispersion from natural sources: application and hazard assessment at Caldara di Manziana, Italy, Geochem. Geophy. Geosy., 9, Q03002, doi:10.1029/2007GC001762, 2008.

Deutsch, C. V. and Journel, A. G.: GSLIB: geostatistical Software Library and User's Guide, Second Edition, Oxford University Press, New York, USA, 369 pp., 1998.

Dobler, J. T., Harrison, F. W., Browell, E. V., Lin, B., McGregor, D., Kooi, S., Choi, Y., and Ismail, S.: Atmospheric CO_2 column measurements with an airborne intensity-modulated continuous-wave 1.57-micron fiber laser lidar, Appl. Optics, 52, 2874–2894, 2013.

Douglas, S. and Kessler, R.: User's Manual for the Diagnostic Wind Model, edited by Carr, L., San Rafael, CA, USA, vol. III, EPA-450/4-90-007C, 1990.

Farrar, C. D., Sorey, M. L., Evans, W. C., Howle, J. F., Kerr, B. D., Kennedy, B. M., King, C.-Y., and Southon, J. R.: Forest-killing diffuse CO_2 emission at Mammoth Mountain as a sign of magmatic unrest, Nature, 376, 675–678, 1995.

Fiorani, L. and Durieux, E.: Comparison among error calculations in differential absorption lidar measurements, Opt. Laser Technol., 3, 371–377, 2001.

Gibert, F., Joly, L., Xuéref-Rémy, I., Schmidt, M., Royer, A., Flamant, P. H., Ramonet, M., Parvitte, B., Durry, G., and Zéninari, V.: Inter-comparison of 2 micron Heterodyne Differential Absorption Lidar, Laser Diode Spectrometer, LICOR NDIR analyzer and flasks measurements of near-ground atmospheric CO_2 mixing ratio, Spectrochim. Acta A, 71, 1914–1921, 2009.

Granieri, D., Costa, A., Macedonio, G., Bisson, M., and Chiodini, G.: Carbon dioxide in the urban area of Naples: contribution and effects of the volcanic source, J. Volcanol. Geoth. Res., 260, 52–61, 2013.

Granieri, D., Carapezza, M. L., Barberi, F., Ranaldi, M., Ricci, T., and Tarchini, L.: Atmospheric dispersion of natural carbon dioxide emissions on Vulcano Island, Italy, J. Geophys. Res. Solid Earth, 119, 5398–5413, 2014.

Grant, W. B., Brothers, A. M., and Bogan, J. R.: Differential absorption lidar signal averaging, Appl. Optics, 27, 1934–1938, 1988.

Hansell, A. L. and Oppenheimer, C.: Health hazards from volcanic gases: a systematic literature review, Arch. Environ. Health, 59, 628–639, 2004.

AMTD
8, 4325–4345, 2015

Kameyama, S., Imaki, M., Hirano, Y., Ueno, S., Kawakami, S., Sakaizawa, D., and Nakajima, M.: Development of 1.6 m continuous-wave modulation hard-target differential absorption lidar system for CO_2 sensing, Opt. Lett., 34, 1513–1515, 2009.

La Spina, A., Burton, M., and Salerno, G.: Unravelling the processes controlling gas emissions from the central and northeast craters of Mt. Etna, J. Volcanol. Geoth. Res., 198, 368–376, 2010.

Naughton, J. J., Derby, J. V., and Glover, R. B.: Infrared measurements on volcanic gas and fume: Kilauea eruption, 1968, J. Geophys. Res., 74, 3273–3277, 1969.

Queißer, M., Burton, M., and Fiorani, L.: Differential absorption lidar for volcanic CO_2 sensing tested in an unstable atmosphere, Opt. Express, 23, 6634–6644, 2015.

Rogie, J. D., Kerrick, D. M., Chiodini, G., and Frondini, F.: Flux measurements of nonvolcanic CO_2 emission from some vents in central Italy, J. Geophys. Res., 105, 8435–8445, 2000.

Rothman, L. S., Gordon, I. E., Babikov, Y., Barbe, A., Benner, D. C., Bernath, P. F., Birk, M, Bizzocchi, L., Boudon, V., Brown, L. R., Campargue, A., Chanc, K., Coudert, L., Devi, V. M., Drouin, B. J., Fayt, A., Flaud, J.-M., Gamache, R. R., Harrison, J., Hartmann, J.-M., Hill, C., Hodges, J. T., Jacquemart, D., Jolly, A., Lamouroux, J., LeRoy, R. J., Li, G., Long, D., Mackie, C. J., Massie, S. T., Mikhailenko, S., Müller, H. S. P., Naumenko, O. V., Nikitin, A. V., Orphal, J., Perevalov, V., Perrin, A., Polovtseva, E. R., Richard, C., Smith, M. A. H., Starikova, E., Sung, K., Tashkun, S., Tennyson, J., Toon, G. C., Tyuterev, V. G., Auwera, J. V., and Wagner, G.: The HITRAN 2012 Molecular Spectroscopic Database, J. Quant. Spectrosc. Ra., 130, 4–50, 2013.

Wooster, M. J., Freeborn, P. H., Archibald, S., Oppenheimer, C., Roberts, G. J., Smith, T. E. L., Govender, N., Burton, M., and Palumbo, I.: Field determination of biomass burning emission ratios and factors via open-path FTIR spectroscopy and fire radiative power assessment: headfire, backfire and residual smouldering combustion in African savannahs, Atmos. Chem. Phys., 11, 11591–11615, doi:10.5194/acp-11-11591-2011, 2011.

AMTD
8, 4325–4345, 2015

Table 1. Key parameters of the DIAL.

Instrument weight	20 kg
Instrument rack size (without telescope)	55 × 35 × 23 cm
System power consumption	Idle 20 W, max. 70 W
Lasers	Two NKT Koheras Basik seed and Boostik amplifier
ON/OFF wavelength	1572.992/1573.160 nm
Laser line width	< 1 kHz (< 1 ppm of CO_2 absorption line width)
Beam full angle divergence	1.7 mrad (used for these tests)
Wavelength stability (ON & OFF)	< 0.04 p.m. (5 MHz)
Wavelength switching rate	1 kHz
Maximum optical power	1.5 W
Telescope	Vixen VMC200L Catadioptric Schmidt–Cassegrain with Al mirrors
Telescope aperture	200 mm
Receiver field of view	1 mrad
Optical filter bandwidth	12 nm
Detector type	InGaAs PIN photodiode
Detector diameter	300 µm
Conversion gain (after TIA)	1e9 V/W
Detector module NEP	13 fW/Hz$^{1/2}$
ADC resolution and rate	24-bit, 50 kHz
Range measurement	Jenoptik DLEM 4k range finder
Range finder accuracy	< 1 m

AMTD
8, 4325–4345, 2015

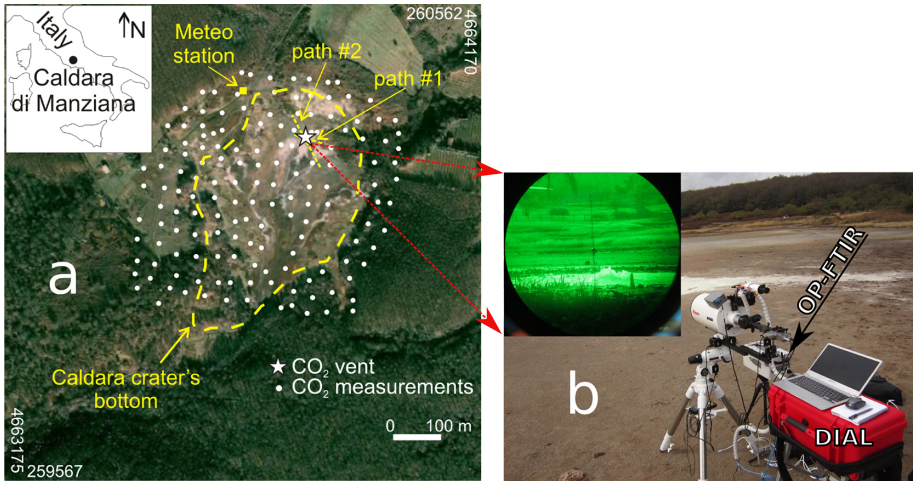

Figure 1. (a) Orthophoto of Caldara di Manziana (CdM) showing the location of the CO_2 measurement points, the target CO_2 vent, the meteorological station, and the FTIR and DIAL paths in dashed yellow (path #1 is 49 m long, path #2 is 126 m long). **(b)** Path #1: DIAL telescope on tall tripod at the beginning of the path with main unit in red box and OP-FTIR on small tripod. Inset: view through telescope finder showing IR source at the end of path, behind water pool (CO_2 vent) at center of crosshair.

AMTD
8, 4325–4345, 2015

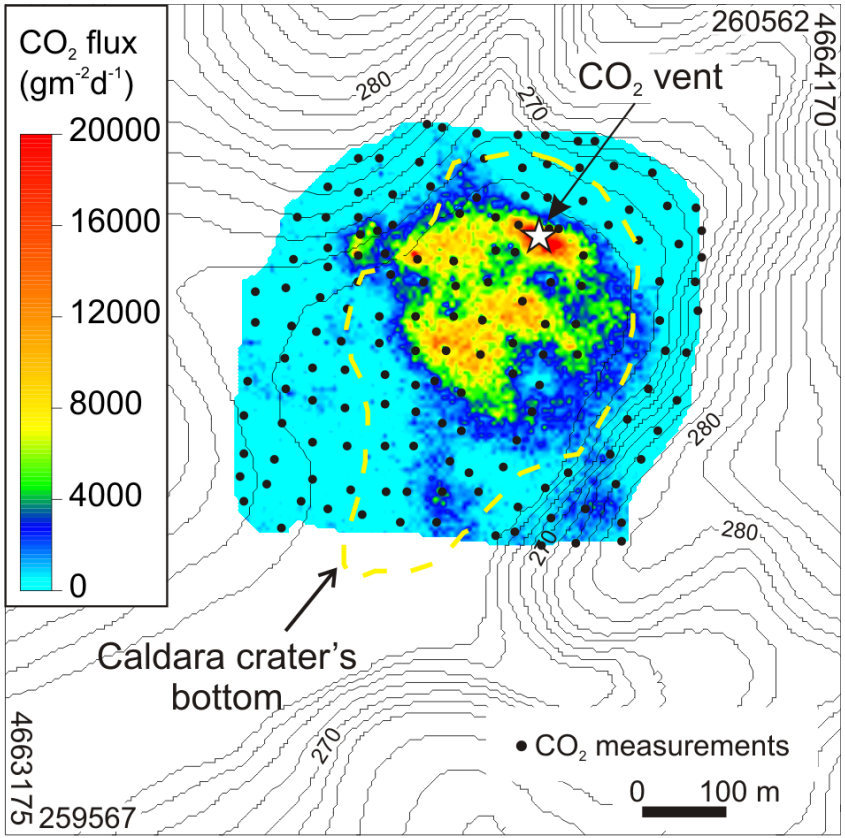

Figure 2. October 2014 map of soil CO_2 flux at Caldara di Manziana. Contour lines mark the height profile.

AMTD
8, 4325–4345, 2015

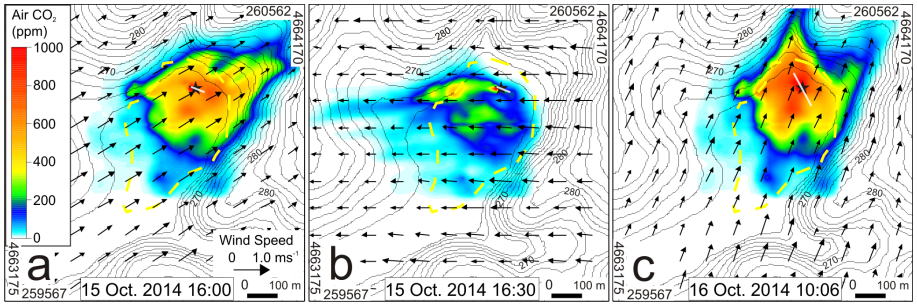

Figure 3. Air CO_2 concentration maps (above the local background level of 370 ppm) at a height of 0.5 m assuming winds blowing from **(a)** 235° N (average speed 1.33 m s^{-1}); **(b)** 88° N (average speed 1.89 m s^{-1}); and **(c)** 203° N (average speed 1.14 m s^{-1}). White strokes mark the OP-FTIR and DIAL paths (path #1 on 15 October and path #2 on 16 October, see Fig. 1) crossing the CO_2 vent (black star). Arrows depict the wind field derived from the Diagnostic Wind Model (DWM). The scales of the maps and wind fields are reported in **(a)**.

AMTD
8, 4325–4345, 2015

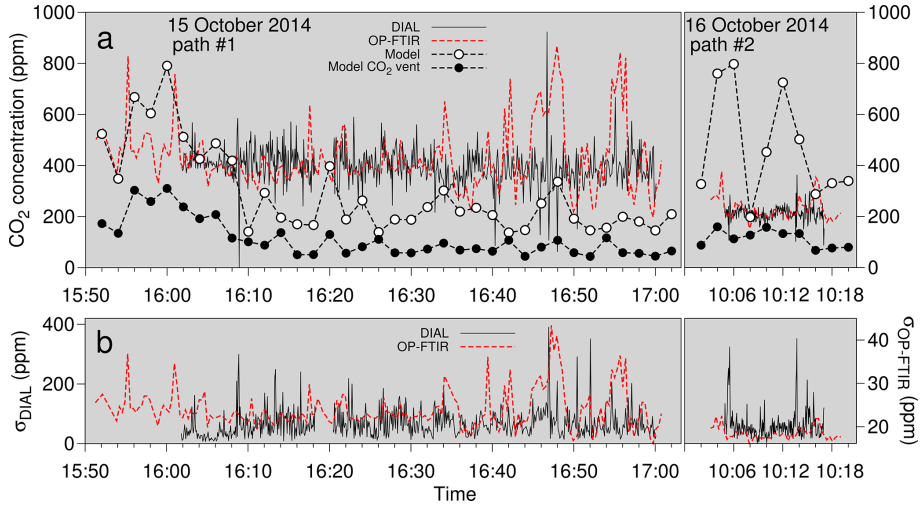

Figure 4. (a) Time series of air CO_2 concentration above the local background level of 370 ppm from DIAL, OP-FTIR and dispersion modeling for path #1 and #2. **(b)** Corresponding SDs of the DIAL and the OP-FTIR results for each measured point.

AMTD
8, 4325–4345, 2015